Title

Non-local heat transport, rotation reversals and up/down impurity density asymmetries in Alcator C-Mod ohmic L-mode plasmas

Journal

Nuclear Fusion, 53(3)

ISSN

0029-5515

Authors

Rice, JE
Gao, C
Reinke, ML
et al.

Publication Date

2013-03-01

DOI

10.1088/0029-5515/53/3/033004

Peer reviewed

PSFC/JA-12-32

Non-local Heat Transport, Rotation Reversals and Up/Down Impurity Density Asymmetries in Alcator C-Mod Ohmic L-mode Plasmas

Rice, J., Gao, C., Reinke, M., Diamond, P.*, Howard, N., Sun, H.**, Cziegler, I.*, Hubbard, A., Podpaly, Y., Rowan, W.***, Terry, J., Chilenski, M., Delgado-Aparicio, L.****, Ennever, P., Ernst, D., Greenwald, M., Hughes, J., Ma, Y., Marmar, E., Porkolab, M., and Wolfe, S.

* CMTFO, San Diego, CA
** SWIP, Chengdu, China
*** University of Texas, Austin, TX
**** PPPL, Princeton, NJ

September, 2012

Plasma Science and Fusion Center
Massachusetts Institute of Technology
Cambridge MA 02139 USA

This work was supported by the U.S. Department of Energy, Grant No. DE-FC02-99ER54512.

Non-local Heat Transport, Rotation Reversals and Up/Down Impurity Density Asymmetries in Alcator C-Mod Ohmic L-mode Plasmas

J.E. Rice, C. Gao, M.L. Reinke, P.H. Diamond[‡♮], N.T. Howard, H.J. Sun[†♮], I. Cziegler[‡], A.E. Hubbard, Y.A. Podpaly, W.L. Rowan[♯], J.L. Terry, M.A. Chilenski, L. Delgado-Aparicio[♭], P.C. Ennever, D. Ernst, M.J. Greenwald, J.W.Hughes, Y. Ma, E.S. Marmar, M. Porkolab and S.M. Wolfe

PSFC, MIT, Cambridge, Massachusetts 02139, USA

[‡]*CMTFO, UCSD, San Diego, California 92903, USA*

[♮]*WCI Center for Fusion Theory, NFRI, Daejeon 305-333, Korea*

[†]*SWIP, Chengdu 610041, China*

[♯]*IFS, The University of Texas at Austin, Austin, Texas 78712, USA*

[♭]*PPPL, Princeton, New Jersey 08543, USA*

Abstract

Several seemingly unrelated effects in Alcator C-Mod Ohmic L-mode plasmas are shown to be closely connected: non-local heat transport, core toroidal rotation reversals, energy confinement saturation and up/down impurity density asymmetries. These phenomena all abruptly transform at a critical value of the collisionality. At low densities in the linear Ohmic confinement regime, with collisionality $\nu_* \leq 0.35$ (evaluated inside of the q=3/2 surface), heat transport exhibits non-local behavior, core toroidal rotation is directed co-current, edge impurity density profiles are up/down symmetric and a turbulent feature in core density fluctuations with k_θ up to 15 cm^{-1} ($k_\theta \rho_s \sim 1$) is present. At high density/collisionality with saturated Ohmic confinement, electron thermal transport is diffusive, core rotation is in the counter-current direction, edge impurity density profiles are up/down asymmetric and the high k_θ turbulent feature is absent. The rotation reversal stagnation point (just inside of the q=3/2 surface) coincides with the non-local electron temperature profile inversion radius. All of these observations can be unified in a model with trapped electron mode prevalence at low collisionality and ion temperature gradient mode domination at high collisionality.

I. Introduction

There are several longstanding mysteries in tokamak research: explanation of the observed edge up/down impurity density asymmetries [1, 2, 3, 4], the mechanism governing the linear Ohmic confinement (LOC, also known as neo-Alcator scaling) regime and the transition to saturated Ohmic confinement (SOC, L-mode) [5, 6, 7, 8, 9, 10, 11, 12, 13, 14, 15, 16, 17], and the underlying cause of 'non-local electron heat transport' following cold pulses [18, 19, 20, 21, 22, 23, 24, 25, 26, 27]. A recent mystery to add to this list is the rotation reversal or inversion process [28, 29, 30, 31, 32, 33], in which the core toroidal rotation abruptly switches direction, with negligible effect on other macroscopic plasma parameters. Rotation reversals constitute a novel form of momentum transport bifurcation and have been induced by changes in the collsionality through the density, plasma current and magnetic field. Recently, the connection among rotation reversals, the transformation from LOC to SOC, saturation of electron density profile peaking and changes in turbulence characteristics has been demonstrated [32, 33, 34, 35]. This connection is extended here to include 'non-local electron heat transport' and up/down impurity density asymmetries [36]. A working hypothesis suggests that many of these observations are consistent with transport dominated by ion temperature gradient (ITG) modes above a critical collisionality, with trapped electron modes (TEMs) prevalent below the critical collisionality. In future reactor grade plasmas, the collisionality will be low so it is important to understand TEM dominant regimes. The outline of the paper follows. In Section II the experimental setup is described and in Section III the results of the cold pulse experiments are shown, including time evolution of the electron and ion temperature profiles, and scalings of relevant plasma parameters with electron density and plasma current. Concomitant changes in the toroidal rotation velocity profiles, energy confinement and up/down impurity density asymmetries are also presented. In Section IV other parameter trends are shown, including turbulence characteristics. A unifying discussion including the competition between CTEM and ITG mode dominance is presented in Section V, followed by a summary.

II. Experimental Setup

This detailed study in Ohmic L-mode plasmas has been performed on the Alcator C-Mod tokamak [37] (major radius R = 0.67 m, typical minor radius of 0.21 m). The experiments described here were carried out in 5.4 T deuterium plasmas, in the lower single null configuration, with elongation $\kappa \sim 1.6$, and upper and lower triangularities of ~ 0.29 and ~ 0.54, respectively. Electron densities were in the range from 0.25 to $1.80\times10^{20}/\mathrm{m}^3$, with plasma currents between 0.55 and 1.1 MA ($5.9 \geq q_{95} \geq 3.2$). Electron densities were determined from a two color interferometer, fast electron temperature evolution using electron cyclotron emission and Z_{eff} from visible *bremsstrahlung* [38]. Toroidal rotation, ion temperature and argon emissivity profiles were measured with a high resolution imaging x-ray spectrometer system [39, 40], and electron density and temperature profiles were provided by Thomson scattering [38].

Cold pulses were achieved by the rapid edge cooling following CaF_2 injection from a unique multi-pulse laser blow-off system [41]. Impurity confinement times following injections were determined from soft x-ray emission profile evolution. Information regarding plasma turbulence was provided by examination of density fluctuations recorded from phase contrast imaging (PCI) and gas puff imaging (GPI) diagnostics [38]. Magnetic flux surfaces were determined from EFIT [42] calculations.

III. Cold Pulse Propagation in SOC and LOC Plasmas, Up/Down Impurity Density Asymmetries and the Relation to Rotation Reversals

Thermal transport has been investigated by means of rapid edge cooling from impurity injection by laser blow-off. Shown in Fig.1 are the time histories of the edge and core electron and ion temperatures in an SOC discharge (5.4 T, 0.8 MA, $q_{95} \sim 4.2$, n_e=1.3×10^{20}/m^3) with a CaF_2 injection at 0.800 s. Following the rapid cooling

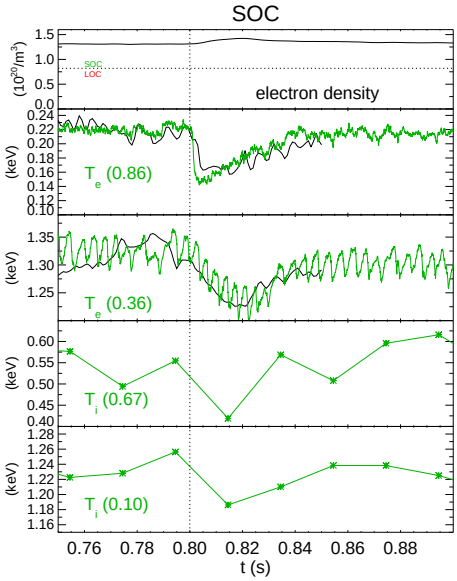

Figure 1: Time histories of the electron density, edge electron temperature, core electron temperature, edge ion temperature and core ion temperature for an SOC discharge with a CaF_2 injection at 0.800 s. (r/a) values for the measurements are indicated by the numbers in parentheses. Simulations of the electron temperature evolution are shown by the thin lines in the second and third frames.

of the edge electron temperature was a drop in the core temperature, on a time scale consistent with the global energy confinement time [16], which for this discharge was about 30 ms. The electron temperature evolution at several radii is shown in Fig.2; a steady progression of the cold pulse from the edge to the plasma center is evident. In this case, the electron thermal transport is well described by a simple diffusion model

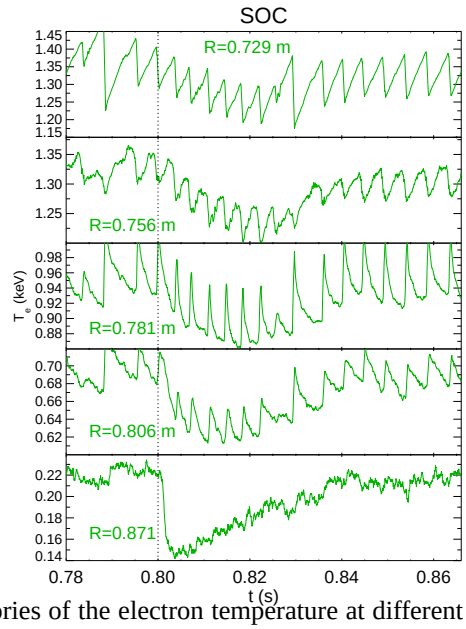

Figure 2: Time histories of the electron temperature at different radii for an SOC discharge with a CaF_2 injection at 0.800 s.

with an electron thermal conductivity (from global analysis) of order 2 m^2/s. The modeled electron temperature evolution at two radii is shown by the thin lines in Fig.1. The electron thermal conductivity (χ_e) profile used in this calculation is shown by the dashed line in Fig.3. For this SOC regime plasma, there were also modest drops in the ion temperature, although the time resolution in this case is not good. In stark contrast is the behavior in a lower density LOC plasma (5.4 T, 0.8 MA, $q_{95} \sim 4.2$, n_e=0.6$\times 10^{20}/m^3$) with an injection time of 1.000 s, as depicted in Fig.4. Following the edge cooling, there was a rapid *increase* of the core electron temperature, on a time scale ($\sim$5 ms) faster than the diffusive time. This effect is suggestive of a short-lived internal transport barrier (ITB), triggered by the sudden increase of the edge temperature gradient, which can be modeled with an abrupt drop in the core electron thermal conductivity [19, 20, 21, 23, 24, 25, 27], and which persists for the duration of the edge cooling ($\sim$30 ms). A model for this transient increase in electron heat transport (a drop in thermal conductivity) is shown in Fig.3, with a 25% drop in χ_e near r/a = 0.3 (solid to dash-dot lines). The match to the observed electron temperature evolution is shown by the thin lines in Fig.4. There was also formation of an ITB in the ion temperature, which developed on a longer time scale; the central T_i reached its peak after 35 ms. The electron temperature evolution at several radii for this LOC discharge is shown in Fig.5. The electron temperature drop is seen only in as far as R = 0.808 m (r/a $\sim$ 0.58); inside of R = 0.784 (r/a $\sim$ 0.47), the temperature *increased* following the edge cooling. The evolution of the electron and ion temperature profiles, demonstrating the transient ITB for the LOC discharge of Figs.4 and 5, is shown in Fig.6. Following the edge cooling at 1.000 s, the electron temperature reached its peak on a fast time scale

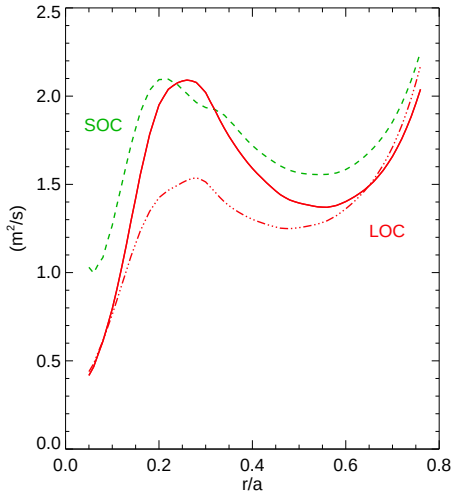

Figure 3: Model electron thermal conductivity for SOC (green dashed) and LOC (solid red to transient dash-dot) plasmas.

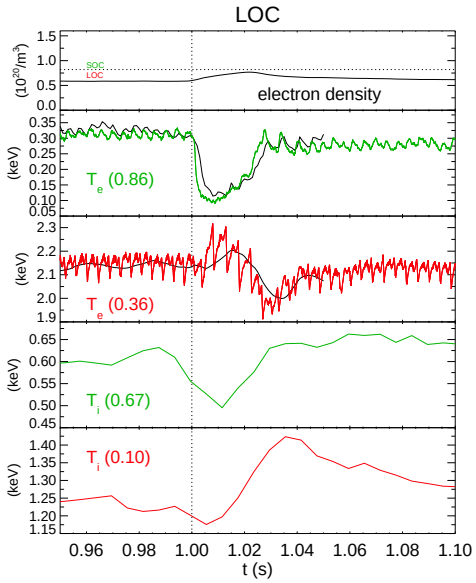

Figure 4: Time histories of the electron density, edge electron temperature, core electron temperature, edge ion temperature and core ion temperature for an LOC discharge with a CaF_2 injection at 1.000 s.

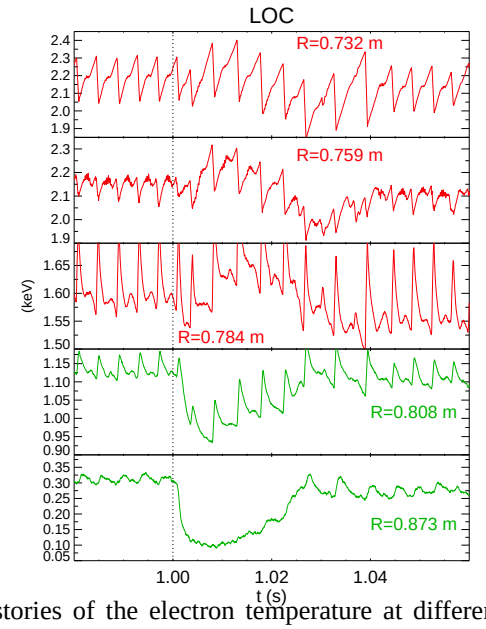

Figure 5: Time histories of the electron temperature at different radii for an LOC plasma with a CaF_2 injection at 1.000 s.

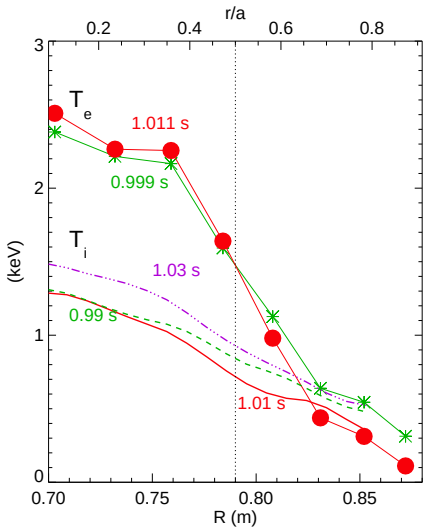

Figure 6: Electron and ion temperature profiles at three characteristic times during an LOC plasma.

of less than 10 ms, and returned to its pre-injection shape after 30 ms. The electron temperature profile shown is from 1.011 s (dots), evaluated during the same phase of the sawtooth oscillations as the profile just before the laser pulse (asterisks). The flex point of the electron temperature profile was near R = 0.79 m (r/a $\sim$ 0.5), marked by the dotted vertical line. R/L$_{Te}$ at this location changed from 9.9 before the injection to 12.0 at 1.011 s. The ion temperature profile evolved on a longer time scale, with a drop in the edge ion temperature occuring when the core electron temperature reached its peak. The central ion temperature attained its maximum when the core electron ITB had disappeared. The normalized ion temperature gradient scale length (R/L$_{Ti}$) at R = 0.79 m changed from 5.0 before the injection to 7.1 at 1.01 s to 5.9 at 1.05 s. For this discharge, the time resolution of the x-ray spectrometer system was 6 ms.

Interestingly the electron temperature profile flex point is very close to the intrinsic toroidal rotation reversal anchor point, as shown in Fig.7. These velocity profiles were

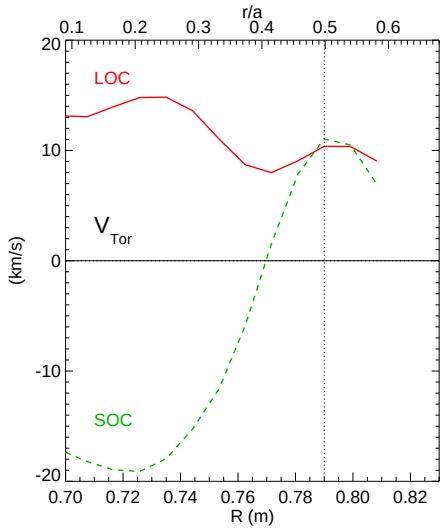

Figure 7: Rotation velocity profiles at two different times for a discharge with a dynamic rotation reversal.

obtained from a discharge (q$_{95}$ $\sim$ 4.2) with a dynamic rotation reversal [32] induced by ramping the electron density from 0.72 to 0.83$\times$10^{20}/m^3. For this plasma current and magnetic field, the rotation reversal anchor point and electron temperature flex point were both located near R = 0.79 m (r/a $\sim$ 0.5). This suggests a connection, likely via a collisionality dependence, between the transient ITB formation (following edge cooling) in LOC plasmas and the intrinsic rotation reversal process. This connection is further emphasized in Fig.8, showing the time evolution of a discharge with an upward density ramp, which crosses the LOC/SOC boundary. At low density, in the LOC regime, the core toroidal rotation was directed co-current, and reversed direction (beginning at 1.2 s) at high density in the SOC regime. This 0.8 MA (q$_{95}$ $\sim$ 4.2) plasma had four CaF_2 injections, at 0.8, 1.0, 1.2 and 1.4 s. The core electron temperature in-

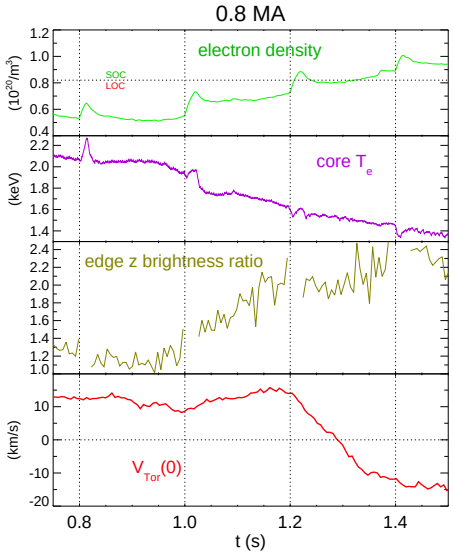

Figure 8: Time histories of the electron density (top), core electron temperature (second frame), edge up/down forbidden line brightness (third frame) and core toroidal rotation velocity (bottom) for a 0.8 MA discharge with a rotation reversal. CaF_2 injection times are shown by the vertical dotted lines.

creased following the cold pulses in LOC (0.8 and 1.0 s), and dropped in SOC at high density (1.4 s), when the rotation was counter-current.

The ion temperature and toroidal rotation velocity profiles of Figs.6 and 7 were obtained from the Doppler broadening and Doppler shift of emission from H- and He-like argon, recorded with a spatially imaging high wavelength resolution x-ray spectrometer system [39, 40]. Argon is introduced into discharges by gas puffing to a level typically of order $10^{-4}n_e$. Example x-ray spectra of He-like Ar^{16+} from the plasma edge are shown in Fig.9. These spectra, obtained for viewing chords tangent to r/a $\sim$ 0.9, include the resonance line, w (1s2p $^1P_1$ -1s^2 $^1S_0$, 3949.28 mÅ), the intercombination lines, x and y (1s2p $^3P_2$ -1s^2 $^1S_0$, 3965.99 mÅ, and 1s2p $^3P_1$ -1s^2 $^1S_0$, 3969.40 mÅ) and the forbidden line, z (1s2p $^3S_1$ -1s^2 $^1S_0$, 3994.28 mÅ). At the low electron temperatures of the edge plasma, the upper levels of these transitions were populated by radiative recombination of H-like argon [43], which was born at the plasma center, and was transported outward on the fast time scale of L-mode impurity confinement [44, 45, 46]. In the top frame, from an LOC plasma, the spectra from the top and bottom viewing chords have the same intensity, and it may be concluded that the edge impurity densities are up/down symmetric. In contrast, in the bottom frame are spectra from an SOC discharge. The spectrum from the chord viewing the top of the plasma is over 2 times brighter than from the bottom viewing chord. Edge emissivity profiles of the forbidden line z from the top and the bottom of the machine for the 0.8 MA SOC discharge are shown in Fig.10. There is an enhancement of the emission from

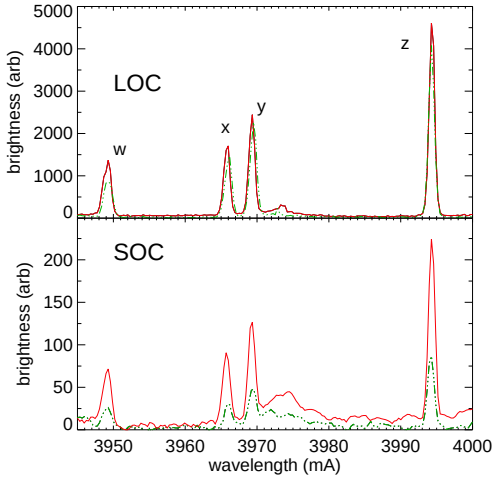

Figure 9: Ar^{16+} spectra for chords tangent to r/a $\sim$ 0.9 viewing the top (solid) and bottom (dash-dot) of the plasma for LOC (top frame) and SOC (bottom frame).

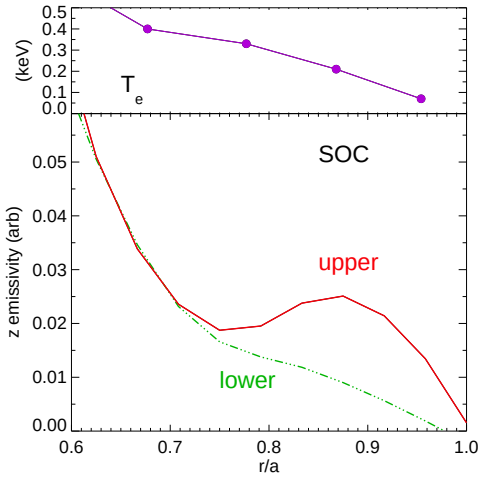

Figure 10: Top frame: edge electron temperature profile. Bottom frame: edge Ar^{16+} forbidden line z emissivity profiles from the top (solid) and bottom (dash-dot) of a 5.4 T, 0.8 MA SOC plasma.

the top of the plasma between 0.8$\leq$ r/a $\leq$ 1.0. This implies that there is an up/down impurity density asymmetry, with an excess at the top of the plasma, in the direction opposite to the ion B$\times\nabla$B drift direction [3, 4]. This enhancement does not depend on the X-point location (upper versus lower null). In the third frame of Fig.8 is shown the time history of the up/down Ar^{16+} forbidden line (z) ratio, evaluated from chords tangent to r/a $\sim$ 0.9 viewing the top and the bottom of the plasma. Up until 1.0 s, in the LOC regime, the impurity density was up/down symmetric (ratio $\sim$ 1); after 1.2 s in the SOC regime, this ratio was in excess of 2. This edge asymmetry precedes the core rotation reversal, occuring at a lower density. This abrupt onset of the up/down impurity density asymmetry following a slight change in the electron density suggests that this is probably not a neo-classical effect.

The relationship among energy confinement, non-local heat transport, core toroidal rotation reversals and particle confinement (including edge up/down impurity density asymmetries) is further demonstrated in Fig.11, obtained from shot-by-shot scans of the electron density in 0.8 MA, 5.4 T ($q_{95} \sim 4.2$) discharges. For this value of q_{95}, there is

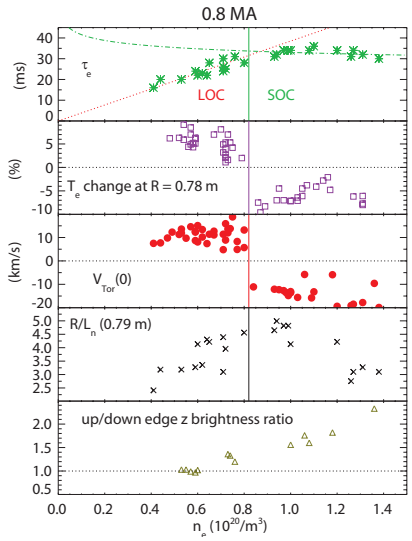

Figure 11: The global energy confinement time (top), percent change in electron temperature at R = 0.78 m following impurity injections (second frame), core toroidal rotation velocity (middle), the inverse density gradient scale length (fourth frame) and up/down edge impurity brightness ratio (bottom) as a function of electron density for 0.8 MA, 5.4 T discharges.

an abrupt change in the direction of the core toroidal rotation velocity (middle frame) from co-current below an electron density of $0.82\times10^{20}/m^3$ to counter-current above. The vertical line indicates this critical density. Also shown is the global energy confinement time (top frame) and the related transition from LOC (dotted line, neo-Alcator scaling [47]) to SOC (dash-dot line, L-mode scaling [48]) is clear [32, 33, 35]. Near

this same critical density there is also a saturation of electron density profile peaking [34, 33], as seen in the fourth frame. Shown in the second frame is the percent change of the electron temperature just inside of the profile flex point (R$\sim$0.79 m, r/a$\sim$0.5 for these conditions, as in Fig.6) evaluated 10 ms following the edge cold pulse. The temperature inside of this radius increases for densities below the rotation reversal and LOC/SOC threshold, and decreases above the critical density; a critical 'non-local' cut-off density has been observed in many experiments [22, 23, 25]. This emphasizes the intimate relationship among 'non-local' heat transport, rotation reversals and confinement saturation. The rotation reversal seems to be the most sensitive indicator of the LOC/SOC transition, since it is easy to detect a change in rotation direction, and this can be determined in a single discharge. In contrast, to ascertain the LOC/SOC transition density, a complete shot-by-shot density scan of the kinetic profiles is required. In the bottom frame of Fig.11 is shown the ratio of the Ar^{16+} forbidden line, z, brightness taken along lines of sight which are tangent to r/a=0.9 from the top and bottom of the plasma. This brightness ratio is indicative of the edge up/down impurity density asymmetry [3, 4]. For low density LOC plasmas, the impurity densities are up/down symmetric, and become asymmetric at higher electron densities, with an impurity density surplus in the direction opposite to the ion B$\times\nabla$B drift direction. The threshold for this behavior is somewhat lower ($\sim 0.6\times 10^{20}/m^3$) than the reversal, LOC/SOC and T_e inversion (non-local cut-off) density, perhaps because this effect is only seen at the plasma edge (r/a$\sim$0.9), well outside of the T_e profile flex and rotation reversal anchor points.

Similar density scans have been carried out for 5.4 T plasmas at 0.55 ($q_{95} \sim 5.8$) and 1.1 MA ($q_{95} \sim 3.3$); the results for the 0.55 MA cases are summarized in Fig.12. For 0.55 MA plasmas at 5.4 T, the critical rotation reversal density is at $0.6\times 10^{20}/m^3$ (middle frame), shown by the vertical line. This is similar to the density of confinement saturation (top frame), the non-local cut-off density (second frame) and the density for saturation of electron density profile peaking (fourth frame). The critical density for the appearance of the up/down impurity density asymmetry (bottom frame) is again somewhat lower than the rotation reversal density. The corresponding results for 1.1 MA plasmas are shown in Fig.13. For this plasma current (at 5.4 T), the rotation reversal density is at $1.14\times 10^{20}/m^3$ (vertical line), which aligns fairly well with the density for energy confinement and density profile peaking saturation. Once again, the onset for the up/down impurity density asymmetry occurs at a lower density. In contrast to the lower current cases however, the non-local cut-off density is not well defined (between 1.24 and $1.36\times 10^{20}/m^3$), and certainly occurs at a slightly higher density than the rotation reversal. This difference (only about 10%) in density is demonstrated in Fig.14, which was from a 1.1 MA discharge with a density ramp, and three CaF_2 injections, at 0.8, 1.1 and 1.4 s. Even though the rotation had reversed sign by 1.3 s (bottom frame), the core electron temperature still increased following the cold pulse at 1.4 s. This indicates that at this high plasma current, there is a slight difference in the critical densities for rotation reversal and non-local cut-off. The results of Figs.11-13 are summarized in Fig.15, showing the critical densities for rotation reversal, non-local cut-off (transient eITB formation), the LOC/SOC transition and edge up/down impurity density profile asymmetry formation, which all increase with plasma current. These effects all occur at a fixed collisionality ($\nu_* \propto n_e\ q_{95}$ = constant). The rotation reversal

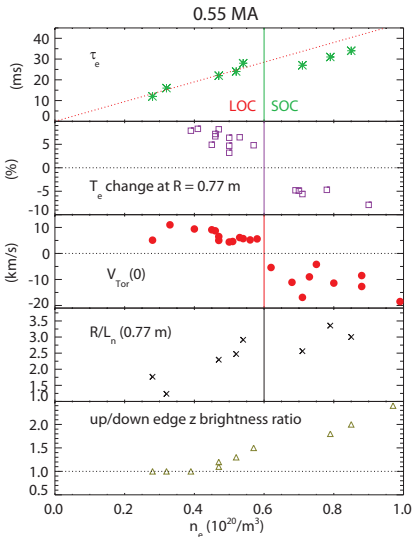

Figure 12: The global energy confinement time (top), percent change in electron temperature at R = 0.77 m following impurity injections (second frame), core toroidal rotation velocity (middle), the inverse density gradient scale length (fourth frame) and up/down edge impurity brightness ratio (bottom) as a function of electron density for 0.55 MA, 5.4 T discharges.

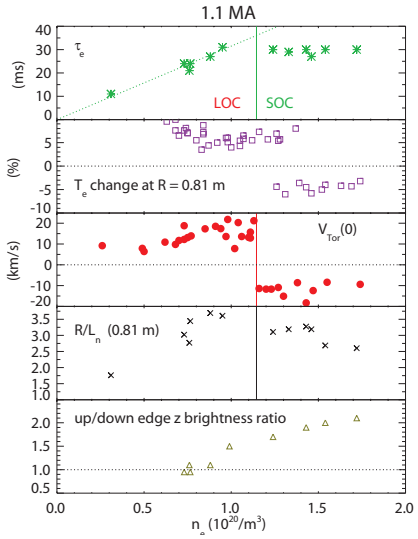

Figure 13: The global energy confinement time (top), percent change in electron temperature at R = 0.81 m following impurity injections (second frame), core toroidal rotation velocity (middle), the inverse density gradient scale length (fourth frame) and up/down edge impurity brightness ratio (bottom) as a function of electron density for 1.10 MA, 5.4 T discharges.

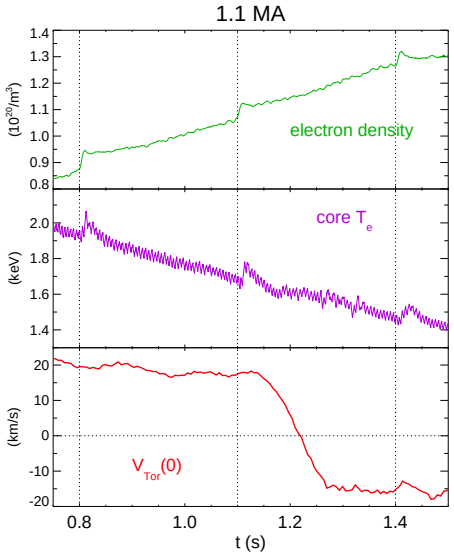

Figure 14: Time histories of the electron density (top), core electron temperature (middle) and core toroidal rotation velocity (bottom) for a 1.1 MA discharge with a rotation reversal. CaF_2 injection times are shown by the vertical dotted lines.

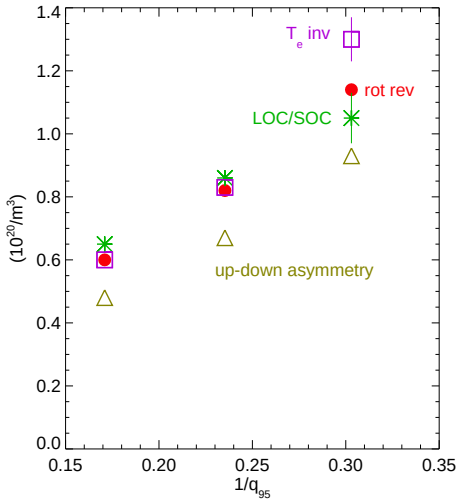

Figure 15: The density for rotation reversal (dots), electron temperature inversion (boxes), LOC/SOC transition (asterisks) and up/down impurity brightness asymmetry (triangles) as a function $1/q_{95}$.

and LOC/SOC transition are well correlated [32, 33, 34, 35], as is the electron temperature non-local cut-off at the lower currents. For the 1.1 MA case ($q_{95}\sim$3.3), the non-local cut-off/temperature inversion/transient eITB persists to a higher density after the rotation reversal and confinement saturation. The up/down impurity density asymmetry follows the same trend but appears systematically at a lower density. This may be because this effect transpires near r/a$\sim$0.9, while the rotation reversal and transient eITB occur more towards the plasma interior. Finally, the close relationship between rotation reversals and electron temperature inversions following cold pulses is further emphasized in Fig.16, which shows the the rotation reversal anchor points and electron temperature profile flex points (as shown in Figs.6 and 7) as a function of $1/q_{95}$. Both of these locations coincide, and move outward with increasing plasma current; outward movement of the T_e profile flex point with increasing $1/q_{95}$ has also been observed in ASDEX Upgrade plasmas [25]. These positions are just inside of the q=3/2 radius as calculated from magnetics reconstructions using EFIT. In order to gauge the accuracy of the q=1 calculations from EFIT, the measured sawtooth inversion radii are shown for comparison.

IV. Other Characteristics near the LOC/SOC Transition

Other relevant parameters of interest have been examined in connection with the LOC/SOC transition, non-local heat transport and rotation reversals. Shown in Fig.17

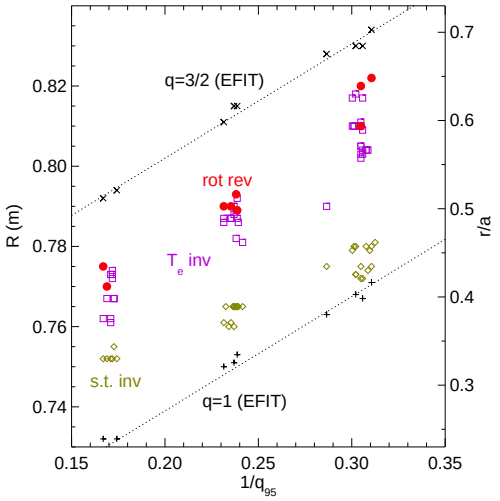

Figure 16: Radial locations of the q=3/2 surface ($\times$s), rotation reversal anchor point (dots), electron temperature profile flex point (boxes), sawtooth inversion radius (diamonds) and q=1 surface (plus signs) as a function of $1/q_{95}$.

are the impurity confinement time, the electron and ion temperatures, and $Z_{\rm eff}$ as a function of electron density for 5.4 T, 0.8 MA ($1/q_{95} \sim 0.24$) discharges. This should be compared with Fig.11. There is no abrupt change in any of these parameters at the rotation reversal critical density (shown by the vertical line), unlike the quantities in Fig.11. In contrast to the global energy confinement time, the global impurity confinement time, determined from the decay of Ca emission following injections using the soft x-ray diode arrays, is rather insensitive to electron density, although there may be a minimum near the critical density. The electron and ion temperatures smoothly converge as the density is raised, and their ratio is about 1.2 at the critical density for these conditions. $Z_{\rm eff}$ also drops smoothly with increasing density, and at the transition has a value of $\sim$3.8 for these 0.8 MA discharges. The dominant intrinsic impurities which contribute to $Z_{\rm eff}$ are boron and molybdenum. Comparable parameter scans for 1.1 MA discharges are shown in Fig.18. Similar behavior is seen for the impurity confinement times, temperatures and $Z_{\rm eff}$, although the temperature ratio and $Z_{\rm eff}$ are slightly lower at the transition since the electron density is higher. The corresponding plot for 0.55 MA plasmas is shown in Fig.19. In this case the values of $Z_{\rm eff}$ and the temperature ratio are higher since the rotation reversal occurs at a lower electron density. The results of these parameter scan for the three different plasma currents are summarized in Fig.20. It is clear from the top two frames that at the critical transition density for each current, the electron to ion temperature ratio and $Z_{\rm eff}$ are not at fixed values. In contrast, the ratio $Z_{\rm eff}/{T_e}^2$ (which figures into the collisionality) at the critical density seems to depend only very weakly on plasma current. The values of these parameters

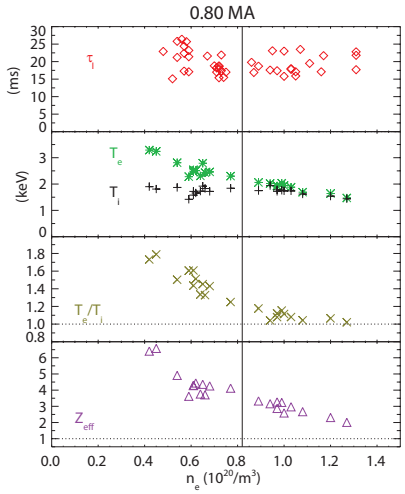

Figure 17: The impurity confinement time (top), the electron and ion temperatures (second frame), the electron to ion temperature ratio (third frame) and $Z_{\rm eff}$ as a function of electron density for 0.8 MA discharges. The vertical lines indicate the rotation reversal density for this current.

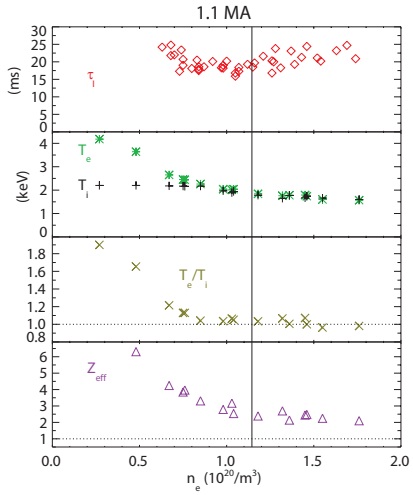

Figure 18: The impurity confinement time (top), the electron and ion temperatures (second frame), the electron to ion temperature ratio (third frame) and $Z_{\rm eff}$ as a function of electron density for 1.1 MA discharges. The vertical lines indicate the rotation reversal density for this current.

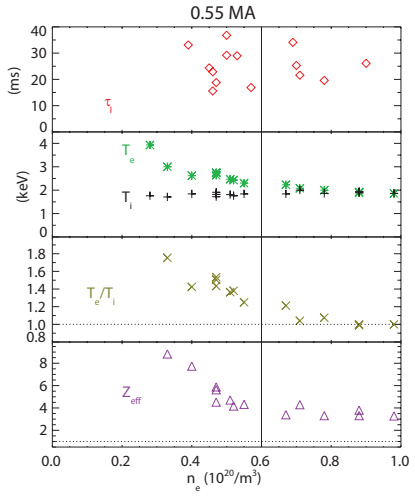

Figure 19: The impurity confinement time (top), the electron and ion temperatures (second frame), the electron to ion temperature ratio (third frame) and $Z_{\rm eff}$ as a function of electron density for 0.55 MA discharges. The vertical lines indicate the rotation reversal density for this current.

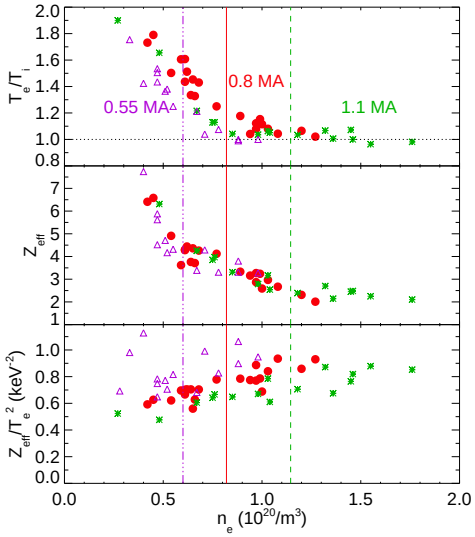

Figure 20: The electron to ion temperature ratio (top), $Z_{\rm eff}$ (middle) and the ratio $Z_{\rm eff}/T_e{}^2$ (bottom) for 0.55 MA (triangles), 0.8 MA (dots) and 1.1 MA (asterisks) plasmas. Vertical lines indicate the rotation reversal density for each current: 0.55 MA (dash-dot), 0.8 MA (solid) and 1.1 MA (dashed).

at the critical density are shown in Fig.21 as a function of $1/q_{95}$ ($\propto I_p$). $Z_{\rm eff}$ at the criti-

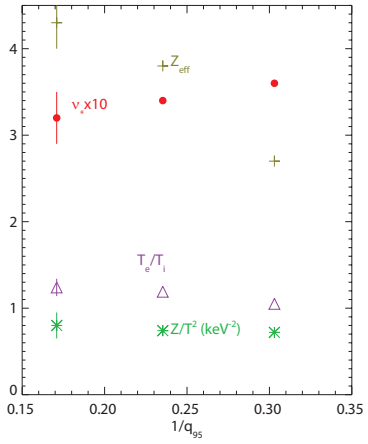

Figure 21: $Z_{\rm eff}$ (plus signs), $\nu_* \times 10$ evaluated at the reversal radius (dots), the electron to ion temperature ratio (triangles) and the ratio $Z_{\rm eff}/T_e{}^2$ (asterisks) at the critical density for rotation reversal as a function of $1/q_{95}$.

cal density drops noticably as the plasma current is raised, while the temperature ratio, $Z_{\rm eff}/T_e{}^2$ and the collisionality ν_* ($\equiv$ 0.0118 q R n_e $Z_{\rm eff}/T_e{}^2$ $\epsilon^{1.5}$, with n_e in $10^{20}/m^3$, R in m and T_e in keV), evaluated at the critical radius, are weak functions of q_{95}. At the critical density, $\nu_* \sim 0.35$, $T_e/T_i \sim 1.2$ and $Z_{\rm eff}/T_e{}^2 \sim 0.8/{\rm keV}^2$.

Turbulence changes at the LOC/SOC transition [49, 50, 15, 51] and during rotation reversals [32, 33, 35] have been well documented. For C-Mod plasmas, a strong feature in density fluctuations suggestive of a trapped electron mode (TEM), with k_θ above 10 cm^{-1} ($k_\theta \rho_s$ extending to 1.0), is present in the core of LOC regime discharges, and which abruptly disappears after the transition to the SOC regime, with collisionality above a critical value. An example case of the conditional spectrum S(k|f) from PCI of the difference in dispersion plots between the LOC phase (n_e=1.08$\times 10^{20}/m^3$) and the SOC phase (n_e=1.13$\times 10^{20}/m^3$) of a 0.9 MA discharge (with a very slight density ramp) is shown in Fig.22. There is a strong feature which is only present in LOC plasmas which extends beyond k_θ = 10 cm^{-1}. Complementary information from the edge plasma is available from GPI, and an example is shown in Fig.23, which consists of conditional spectra of density fluctuations from gas puff imaging views just inside of the last closed flux surface (LCFS). In the top frame, from a discharge in the LOC regime, there is a clear feature with negative k_θ, which indicates a poloidal phase velocity of $\sim$2 km/s, in the ion diamagnetic direction in the lab frame. In SOC plasmas (lower frame), a different feature appears, which has a phase velocity of $\sim$5 km/s in the electron diamagnetic direction in the lab frame. This indicates that there are also

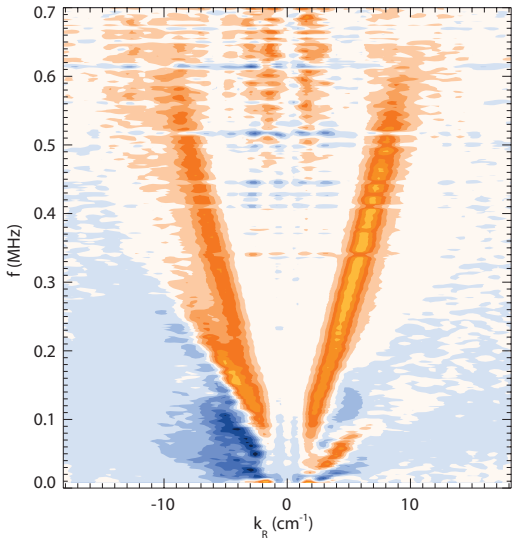

Figure 22: Conditional spectrum of core density fluctuations from PCI of the difference between spectra from the LOC and SOC regime phases of a q_{95} = 3.9 plasma.

changes in edge turbulence at the LOC/SOC transition.

During the transient ITB formation following cold pulses in LOC plasmas, there is a transient down/up edge impurity density asymmetry. Shown in Fig.24 are the time histories of the argon forbidden line brightnesses at r/a $\sim$ 0.9 from views of the top and bottom of the LOC plasma of Fig.4. Immediately after the CaF_2 injection at 1.000 s there was an increase in the brightness from the bottom of the plasma, followed by a decrease in the top brightness. This transient is opposite to the steady up/down impurity density asymmetry observed in SOC plasmas. This behavior in LOC plasmas is not due to changes in the argon source, since the forbidden line intensity depends on the H-like argon density, which must come from outward transport of core argon, and therefore must be due to a change in transport. An interesting feature is the delay in the drop in signal from the top of the plasma compared to the rise at the bottom.

V. Discussion

Rotation reversals on C-Mod occur with nq_{95} = constant [32, 33, 35]. Confinement saturation on many devices (with similar aspect ratio) appears to occur with the product $nq_{95}R \sim$ constant [35], which is consistent with $\nu_* \sim$ constant, since for C-Mod at least, $Z_{eff}/T_e{}^2$ is constant at the transition, as shown in Fig.21. Similarly, the non-

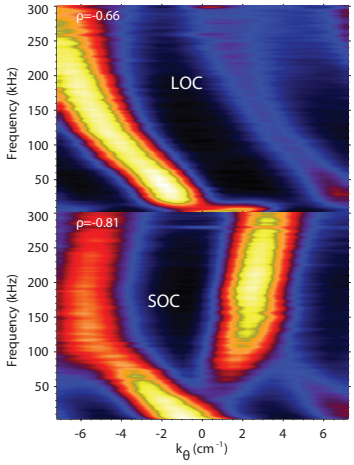

Figure 23: Conditional spectra of density fluctuations from gas puff imaging just inside of the LCFS. top frame- LOC plasma, bottom frame- SOC plasma.

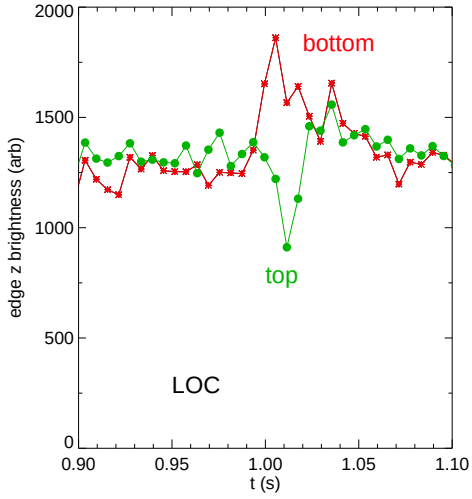

Figure 24: Time histories of the Ar^{16+} z line brightness along chords tangent to r/a $\sim$ 0.9 from the bottom (asterisks) and top (dots) of an SOC plasma. The CaF_2 injection time was 1.000 s.

local cut-off on several machines is observed with $nq_{95}R \sim$ constant as demonstrated in Fig.25, which is a plot of the product of the non-local cut-off density and q_{95}, as a function of major radius R. Except for the RTP point, the trend follows 1/R; it's

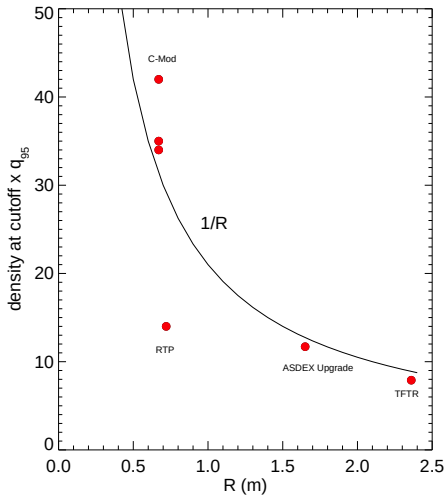

Figure 25: The product of the non-local cut-off density $\times$ q_{95} as a function of machine major radius. The solid curve is proportional to 1/R.

possible that for RTP plasmas, $Z_{\rm eff}/T_e{}^2$ was different than the values from the other devices.

The results of this paper suggest a unified explanation of several seemingly disparate elements of Ohmic L-mode confinement phenomenology, which is summarized in Table I. Central to this unification is the idea that above a critical collisionality, electron-ion collisional thermal coupling will become sufficient to trigger the excitation of ion temperature gradient (ITG) modes, causing a transition from collisionless TEM (CTEM) to ITG dominated turbulence. For this to occur, the coupled power must be comparable to the power transported by CTEMs. Evidence for this CTEM to ITG transition includes changes in both macroscopic parameters and in fluctuation characteristics, and the explanation of several other results follows directly. First, the disappearance of electron 'non-locality' phenomena in SOC is a consequence of the fact that electron thermal power transfer exceeds power transport, effectively eliminating any electron transport dynamics. In the SOC regime, the power is carried by neo-classical processes and by ITG modes, so that any non-locality should appear in the ion channel [52]. This may not be visible due to time resolution constraints. Second, rotation reversal results as a consequence of a change in the sign of the turbulent residual stress, Π^{res}, the gradient of which sets the intrinic torque. Π^{res} is predicted to change sign with the turbulent propagation direction [53] (i.e. electron to ion diamagnetic, as CTEM goes to ITG), consistent with the observation of reversal. Third,

phenomenon	explanation
LOC to SOC transition	change from CTEM to ITG dominance
Change of turbulence propagation direction	change from CTEM to ITG dominance
Electron non-locality and cutoff	Transient CTEM ITB, suppressed by collisional coupling
Rotation reversal	Change in Π^{res} with switch from CTEM to ITG
Saturation in density profile peaking	unclear, CTEM to ITG?
Up/down impurity density asymmetry	up/down asymmetry in ITG intensity due to zonal flow shearing

Table 1: Summary of observed phenomena and commonality.

density profile peaking is observed to saturate at the CTEM to ITG transition [54]. This is inconsistent with the behavior of the convective particle flux, which is predicted to be outward for CTEM but inward for ITG (i.e. flips sign with mode propagation direction). The disparity may likely be due to a strongly enhanced turbulence level, and thus diffusivity, in the ITG regime. An enhanced diffusivity could overcome a reversal in the convective velocity. Fourth, an up/down impurity density asymmetry develops with SOC. This may be a consequence of the appearance of robust, ITG turbulence driven zonal flows, which develop in the SOC regime. Gyro-kinetic simulations suggest that ITG driven zonal flows are larger scale, and more temporaly coherent, than CTEM zonal flows [55]. In the SOC case, a coherent zonal E$\times$B shear should develop, and then cause a coherent eddy shift and tilt (position space), and thus an up/down asymmetry (in ballooning space). An up/down asymmetry in turbulence intensity should then leave a footprint as an up/down asymmetry in impurity density. Comparative Doppler backscattering studies of zonal flows in the LOC and SOC regimes may be used to test this hypothesis.

VI. Conclusions

In summary, the appearance of 'non-local' heat transport, core toroidal rotation reversals, Ohmic energy confinement saturation, edge up/down impurity density asymmetries and turbulence changes appear to be related. Below a critical value of the collsionality, in the LOC regime, electron heat transport is 'non-local', the core intrinsic rotation is directed co-current and the edge impurity density profiles are up/down symmetric. Above this critical collisionality, in the SOC regime, electron heat transport is diffusive, the rotation is counter-current and the edge impurity density profiles are up/down asymmetric. These results are consistent with a change in turbulence domination from CTEMs to ITG modes above a critical collisionality.

VII. Acknowledgements

The authors thank J.Irby for electron density measurements, B.Granetz for soft x-ray measurements, C.Fiore for neutron measurements and the Alcator C-Mod op-

erations group for expert running of the tokamak. Work supported at MIT by DoE Contract No. DE-FC02-99ER54512 and in part by an appointment to the US DOE Fusion Energy Postdoctoral Research Program administered by ORISE.

References

[1] J.L.Terry *et al.*, 1977 *Phys. Rev. Lett.* **39** 1615.

[2] K.Brau *et al.*, 1983 *Nucl. Fusion* **23** 1657.

[3] J.E.Rice *et al.*, 1997 *Nucl. Fusion* **37** 241.

[4] M.L.Reinke, 2011 Ph.D. thesis M.I.T.

[5] R.R.Parker *et al.*, 1985 *Nucl. Fusion* **25** 1127.

[6] R.V.Bravenec *et al.*, 1985 *Plasma Phys. Contr. Fusion* **27** 1335.

[7] Y.Shimomura *et al.*, 1987 'Empirical Scaling of Energy Confinement Time of L-Mode and Optimized Mode and Some Consideration of Reactor Core Plasma in Tokamak' JAERI Report 87-080.

[8] S.Sengoku and the JFT-2M Team, 1987 *J. Nucl. Materials* **145-147** 556.

[9] F.X.Söldner *et al.*, 1988 *Phys. Rev. Lett.* **61** 1105.

[10] F.Alladio *et al.*, 1990 *Plasma Physics and Controlled Nuclear Fusion Research Proc. 13th Int. Conf.* (Washington) Vol. 1 (Vienna: IAEA) p.153.

[11] X.Garbet *et al.*, 1992 *Controlled Fusion and Plasma Physics, Proc. 19th European Conf.* (Innsbruck) Vol. 16C p.107.

[12] F.Wagner and U.Stroth, 1993 *Plasma Phys. Contr. Fusion* **35** 1321.

[13] F.Ryter *et al.*, 1994 *Plasma Phys. Contr. Fusion* **36** A99.

[14] G.Bracco and K.Thomsen, 1997 *Nucl. Fusion* **37** 759.

[15] C.L.Rettig *et al.*, 2001 *Phys. Plasmas* **8** 2232.

[16] M.Greenwald *et al.*, 2007 *Fusion Sci. Technol.* **51** 266.

[17] L.Lin *et al.*, 2009 *Plasma Phys. Contr. Fusion* **51** 065006.

[18] M.W.Kissick *et al.*, 1994 *Nucl. Fusion* **34** 349.

[19] K.Gentle *et al.*, 1995 *Phys. Rev. Lett.* **74** 3620.

[20] K.W.Gentle *et al.*, 1995 *Phys. Plasmas* **2** 2292.

[21] M.W.Kissick *et al.*, 1996 *Nucl. Fusion* **36** 1691.

[22] M.W.Kissick *et al.*, 1998 *Nucl. Fusion* **38** 821.

[23] P.Mantica *et al.*, 1999 *Phys. Rev. Lett.* **82** 5048.

[24] P.Galli *et al.*, 1999 *Nucl. Fusion* **39** 1355.

[25] F.Ryter *et al.*, 2000 *Nucl. Fusion* **40** 1917.

[26] G.M.D.Hogeweij *et al.*, 2000 *Plasma Phys. Contr. Fusion* **42** 1137.

[27] Hong-Juan Sun *et al.*, 2010 *Plasma Phys. Contr. Fusion* **52** 045003.

[28] A.Bortolon *et al.*, 2006 *Phys. Rev. Lett.* **97** 235003.

[29] B.P.Duval *et al.*, 2007 *Plasma Phys. Contr. Fusion* **49** B195.

[30] J.E.Rice *et al.*, 2008 *Plasma Phys. Contr. Fusion* **50** 124042.

[31] B.P.Duval *et al.*, 2008 *Phys. Plasmas* **15** 056113.

[32] J.E.Rice *et al.*, 2011 *Nucl. Fusion* **51** 083005.

[33] J.E.Rice *et al.*, 2011 *Phys. Rev. Lett.* **107** 265001.

[34] C.Angioni *et al.*, 2011 *Phys. Rev. Lett.* **107** 215003.

[35] J.E.Rice *et al.*, 2012 *Phys. Plasmas* **19** 056106.

[36] J.E.Rice *et al.*, 2012 *Phys. Rev. Lett.* submitted.

[37] E.S.Marmar *et al.*, 2007 *Fusion Sci. Technol.* **51** 261.

[38] N.P.Basse *et al.*, 2007 *Fusion Sci. Technol.* **51** 476.

[39] A.Ince-Cushman *et al.*, 2008 *Rev. Sci. Instrum.* **79** 10E302.

[40] M.L.Reinke *et al.*, 2012 *Rev. Sci. Instrum.* submitted

[41] N.T.Howard *et al.*, 2010 *Rev. Sci. Instrum.* **82** 033512.

[42] L.L.Lao *et al.*, 1985 *Nucl. Fusion* **25** 1611.

[43] J.E.Rice *et al.*, 1987 *Phys. Rev. A* **35** 3033.

[44] J.E.Rice *et al.*, 1995 *J. Phys. B.* **28** 893.

[45] J.E.Rice *et al.*, 1997 *Phys. Plasmas* **4** 1605.

[46] J.E.Rice *et al.*, 2007 *Fusion Sci. Technol.* **51** 357.

[47] R.J.Goldston, 1984 *Plasma Phys. Contr. Fusion* **26** 87.

[48] P.N.Yushmanov *et al.*, 1990 *Nucl. Fusion* **30** 1999.

[49] R.L.Watterson *et al.*, 1985 *Phys. Fluids* **28** 2857.

[50] D.L.Brower *et al.*, 1987 *Phys. Rev. Lett.* **59** 48.

[51] G.D.Conway *et al.*, 2006 *Nucl. Fusion* **46** S799.

[52] J.D.Callen *et al.*, 1997 *Plasma Phys. Contr. Fusion* **39** B173.

[53] P.H.Diamond *et al.*, 2009 *Nucl. Fusion* **49** 045002.

[54] X.Garbet *et al.*, 2003 *Phys. Rev. Lett.* **91** 035001.

[55] Jianying Lang *et al.*, 2008 *Phys. Plasmas* **15** 055907.